Supporting Information

Photoactive Zn-Air-Batteries Using Spinel-Type Cobalt Oxide as a Bifunctional Photocatalyst at the Air Cathode

Chanikarn Tomon[a], *Sangchai Sarawutanukul*[a], *Salatan Duangdangchote*[a], *Atiweena Krittayavathananon*[a], *and Montree Sawangphruk*[a,*]

[a] Centre of Excellence for Energy Storage Technology (CEST), Department of Chemical and Biomolecular Engineering, School of Energy Science and Engineering, Vidyasirimedhi Institute of Science and Technology, Rayong 21210, Thailand. E-mail: montree.s@vistec.ac.th
* Corresponding author: montree.s@vistec.ac.th

Section 1: Experimental

Chemicals and materials. All chemicals used in this work are analytical grade and used without any further purification. The cobalt (II) nitrate hexahydrate ($Co(NO_3)_2 \cdot 6H_2O$), urea (CH_4N_2O), and potassium hydroxide (KOH) pellet were acquired from UNIVAR (Downers Grove, Illinois, USA). The ammonium chloride (NH_4Cl) was bought from CARLO ERBA (Chaussée du Vexin, FR). The carbon black was marketed from ALFA AESAR (Lancashire, UK). The poly (vinylidene fluoride) (PVDF) and zinc (II) acetate dihydrate ($Zn(CH_3COO)_2 . 2H_2O$) were obtained from SIGMA-ALDRICH (Missouri, USA). For the chemical solvent, acetone (C_3H_6O) and ethanol (C_2H_5OH) were acquired from ACI LABSCAN (Dhaka, BD). *N*-Methyl-2-pyrrolidone (NMP) was brought from SIGMA-ALDRICH (Missouri, USA). Deionized water (DI) was purified by Milli-Q-system (15 MΩ cm, Millipore, Billerica, MA).

Preparation of spinel-type cobalt oxide (Co_3O_4). Cobalt oxide (Co_3O_4) was synthesized using a two-step synthesis through the hydrothermal method followed by the calcination.[1] Briefly, cobalt hydroxide carbonate ($Co(OH)(CO_3)_{0.5}$) was first produced via a hydrothermal process.[2-6] 0.583 g (2 mmol) of cobalt (II) nitrate hexahydrate ($Co(NO_3)_2 \cdot 6H_2O$), 0.024 g (8 mmol) of ammonium chloride (NH_4Cl) and 0.6 g (10 mmol) of urea (CH_4N_2O) were dissolved in 50 mL DI water, and vigorously stirred for 10 min. The mixing solution was then transferred to a Teflon-lined stainless-steel autoclave (capacity 100 mL). Finally, the autoclave was closed and kept inside an oven at 100^{o}C for 6 h. The reaction is followed by the reactions (S1-4). After the complete reaction, the pink solid product of $Co(OH)(CO_3)_{0.5}$ was obtained. The product was then washed with DI water and ethanol several times via centrifugation– redispersion cycles, and then dried in the oven at 60^{o}C for 24 h.

$$H_2NCONH_2 + H_2O \rightarrow 2NH_3 + CO_2 \quad \text{(S1)}$$

$$CO_2 + H_2O \rightarrow CO_3^{2-} + 2H^+ \quad \text{(S2)}$$

$$NH_3 + H_2O \rightarrow NH_4^+ + OH^- \quad \text{(S3)}$$

$$Co^{2+} + OH^- + 0.5CO_3^{2-} \leftrightarrow Co(OH)(CO_3)_{0.5} \quad \text{(S4)}$$

The $Co(OH)(CO_3)_{0.5}$ precursor on heating decomposes to form cobalt oxides (Co_3O_4). According to TGA and DSC under O_2 environment, the $Co(OH)(CO_3)_{0.5}$ starts to transform at 300^{o}C and has been completely oxidized to the cobalt oxides at *ca*. 500^{o}C.[7-9] Then, in this work, the as-prepared $Co(OH)(CO_3)_{0.5}$ was calcined at 500^{o}C in the air atmosphere for 2 h with a heating rate of 10^{o}C min^{1-}.

Morphological and Structural characterizations. The morphological structure of the $Co(OH)(CO_3)_{0.5}$ and Co_3O_4 was investigated by Field-emission scanning electron microscopy

(FESEM, JSM-7001F, JOEL Ltd., JP) and transmission electron microscopy (TEM, FEI Tecnai G2 20, JEOL Ltd., JP). The crystallinity information was obtained from X-ray diffraction (XRD, PHILIPS, X'Pert-MPD 40 kV 35 mA, Cu Kα 1.54056 Å). The N_2 adsorption-desorption isotherms of the obtained materials were measured by 3Flex3500 (Micromeritics, USA). Furthermore, the electronic properties such as optical band gap energy and the work function of the Co_3O_4 were studied by using UV-Visible near IR spectrometer (UV/Vis/NIR, Lambda 1050, PerkinElmer, USA) and Ultraviolet photoelectron spectrometer (UPS, Riken Keiki, JP). Finally, the oxidation states of Co_3O_4 under dark condition and light illumination were investigated by *ex-situ* Co K-edge fluorescent X-ray absorption spectroscopy (XAS) at Synchrotron Light Research Institute BL.8 (Public Organization), Thailand. Note, XAS has equipped with Ge (220) double-crystal monochromator with an energy range of 3440-12100 eV.

Preparation of Co_3O_4/ITO as the air cathode. The Co_3O_4 ink was mixed with carbon black and PVDF in the ratio of 8 (16 mg): 1 (2 mg): 1 (2 mg) in the NMP solution (1 ml). The ink was continuously stirred for 2 h. Then 0.25 ml of the as-prepared ink (4 mg of the active material) was dropped on an indium-doped tin oxide (ITO) glass (Greatcell Solar Ltd., Australia) with an area of 2x2 cm^2. The solvent was allowed to evaporate at 50 ^oC.

Fabrication of ZABs. Zn-air batteries (ZABs) composes of two electrodes; the Co_3O_4/ITO (2 x 2 cm^2) is used as a cathode and Zn plate (2 x 2 cm^2) with 50 μm thickness is used as an anode. The two electrodes were parallel placed in the electrolyte (6 M KOH + 0.2 M $Zn(CH_3CO_2)_2{\cdot}2H_2O$). The distance between the two electrodes is *ca*. 1 cm. The electrodes and electrolyte were placed in the glass container (5x5 cm^2). One side of the glass container is a quartz window which is placed in between a photoactive Co_3O_4/ITO cathode and a light source. The cell configuration is shown in Figure 1.

Electrochemical evaluations. The electrochemical measurement was performed by the Metrohm AUTOLAB potentiostat (PGSTAT 302N) and controlled via NOVA software 1.11. To study oxygen evaluation, a three-electrode system was set, and the electrochemical response was recorded via cyclic voltammetry (CV) and linear sweep voltammetry (LSV) under dark, and visible light illumination. The visible light (100 mW cm^{-2}) was used as light sources. The Co_3O_4/ITO electrode was used as the working electrode. The saturated calomel electrode (Hg_2Cl_2) and Pt rod were used as the reference and counter electrodes, respectively. The 0.1 M KOH was used as an electrolyte. Note that before measurement all solutions were eliminated impurity gas by purging N_2 for 10 min.

ZABs was also performed under dark condition and light illumination. The specific capacity was calculated based on the mass of the consumed Zn at the current density of 6 mA cm^{2-}. The long-term stability test was determined by galvanostatic method. The profile was discharged for 2 h with a subsequent 2 h of the charging process (4 hours per cycle) at the current density of 2 mA cm^{2-}. All these experiments were performed in the O_2-saturated.

Differential electrochemical mass spectrometry (DEMS). Differential mass spectrometry combined with the conventional DEMS cell (HPR-40, HIDEN ANALYTICAL, Warrington, UK) with the MASsoft Version 7 software was used in this study to detect the volatile products and intermediates which are produced during oxygen evaluation reaction. The DEMS measurement was set by the three-electrode system. The Co_3O_4 was used as the working electrode. The saturated calomel electrode (Hg_2Cl_2) and Pt rod were used as the reference and counter electrodes, respectively. The DEMS was performed together with the chronoamperometry in 1 M KOH electrolyte during applying the potentials stepped from 0.7-2.0 V (V *vs*. RHE). Note, to reach the steady state, each step potential was held for 10 min. The obtained ionic mass current of O_2 at m/z = 32 in various applied potentials is plotted as shown in Figure S5.

Density of state (DOS) determination. The calculations reported in this article were performed by Quantum Espresso Package[10] based on a periodic plane-wave density functional theory (DFT). The interaction between ion cores and valence electrons was accounted by the projector-augmented wave (PAW)[11] pseudopotentials. The exchange and correlation interactions between electrons were treated within the generalized gradient approximation (GGA)[12] with the Perdew-Burke-Ernzerhof (PBE)[13] parameterization. The effect of 3d electron correlation can be improved by considering on-site Coulomb (U) and exchange (J) interactions. An on-site Hubbard term U−J[14] of 6.7, and 4.4 eV[15] were applied for Co^{3+}, and Co^{2+} ions, respectively. The cut-off energy for an expanded plane-wave basis set was set to 20 Ry. The Brillouin zone integration was sampled grid using the 8 x8 x 8 *k*-points mesh for bulk. The optimized lattice constants of the bulk unit cell are obtained as $a = b = c = 8.064$ Å. The value is in good agreement with the experimental values, $a_{exp} = b_{exp} = c_{exp} = 8.065$ Å obtained from XRD (Figure 1c), and from other previous works ($a_{exp} = b_{exp} = c_{exp} = 8.086$ Å)[16].

Section 2: Cobalt Hydroxide Carbonate ($Co(OH)(CO_3)_{0.5}$)

The morphology of $Co(OH)(CO_3)_{0.5}$ was characterized by SEM and TEM techniques as shown in Figure S1 (a-b). Both SEM and TEM images indicate the microrod structure with the smooth surface. The XRD pattern (Figure S1(c)) shows the obvious peaks at $2\theta = 9.9^o$, 17.3^o, 26.5^o, 33.7^o, 35.3^o, 36.4^o, 39.5^o, 44.2^o, 47.0^o, 54.2^o, 55.7^o, 59.4^o and 61.9^o corresponding to (100), (020), (220), (221), (040), (301), (231), (050), (340), (060), (142), (412) and (450), respectively.[2, 3] The diffraction peak is the characteristic peak of the orthorhombic cobalt hydroxide carbonate (JCPDS card, no. 48-0083) with the lattice parameters of $a = 8.914$, $b = 10.294$ and $c = 4.458$A°.

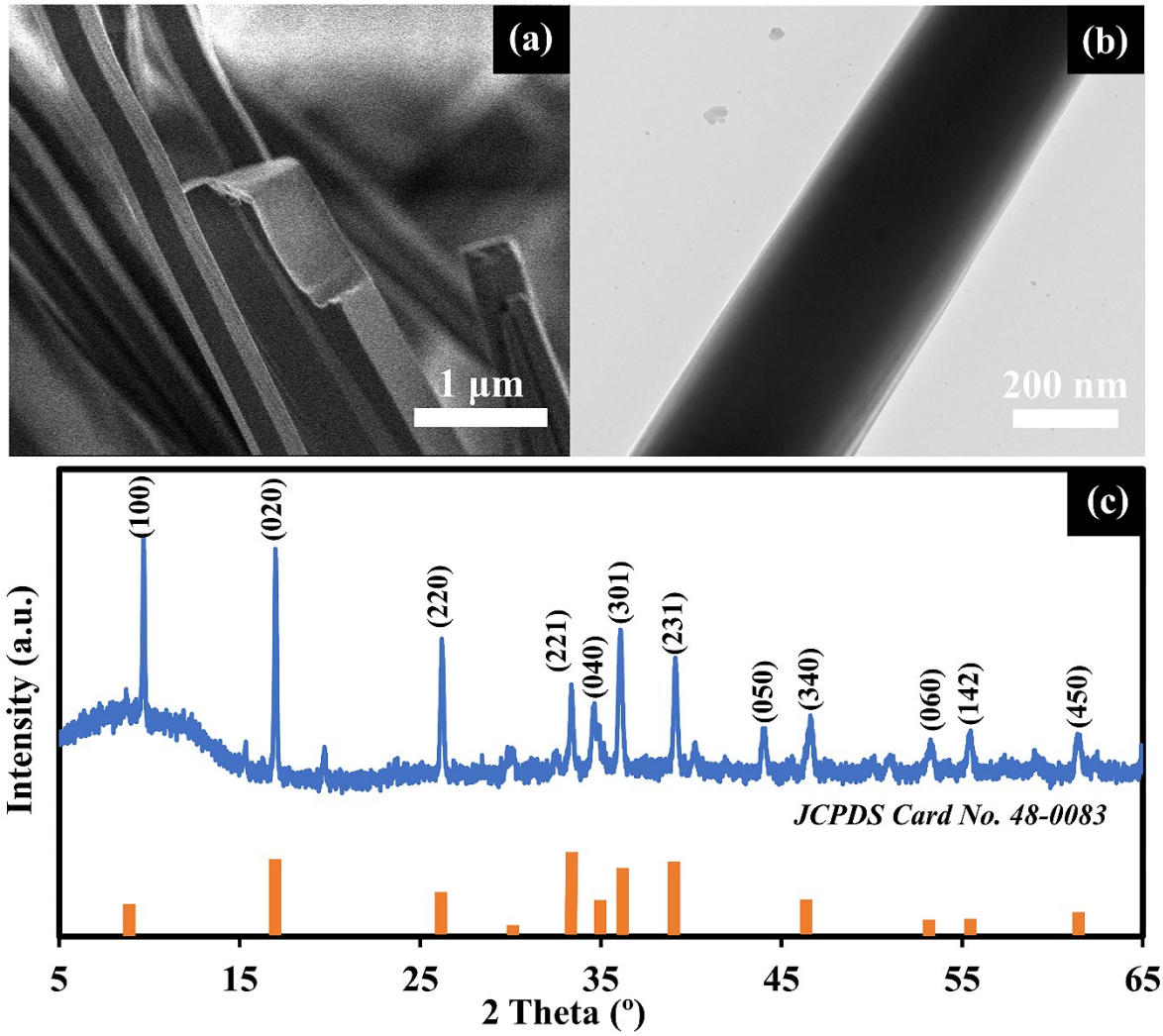

Figure S1. (a) SEM image, (b) TEM image, and (c) XRD pattern of $Co(OH)(CO_3)_{0.5}$.

Section 3: Supporting Figures and Tables

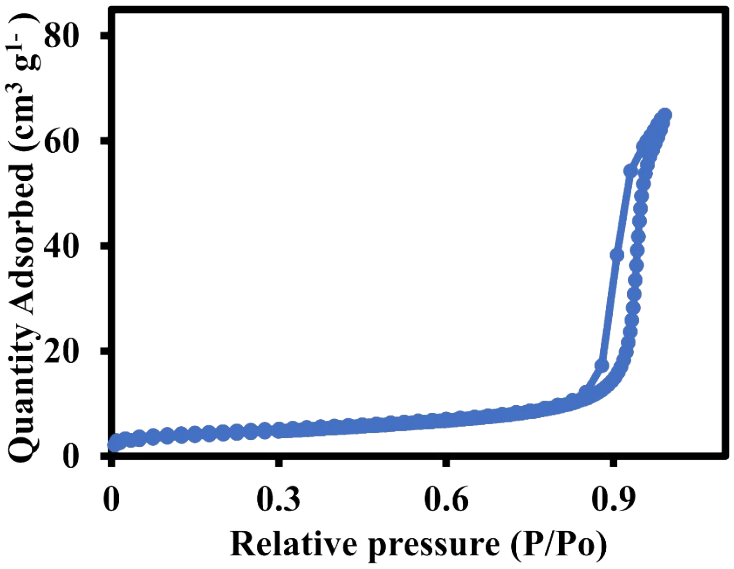

Figure S2. The BET adsorption–desorption isotherm of the as-prepared Co_3O_4

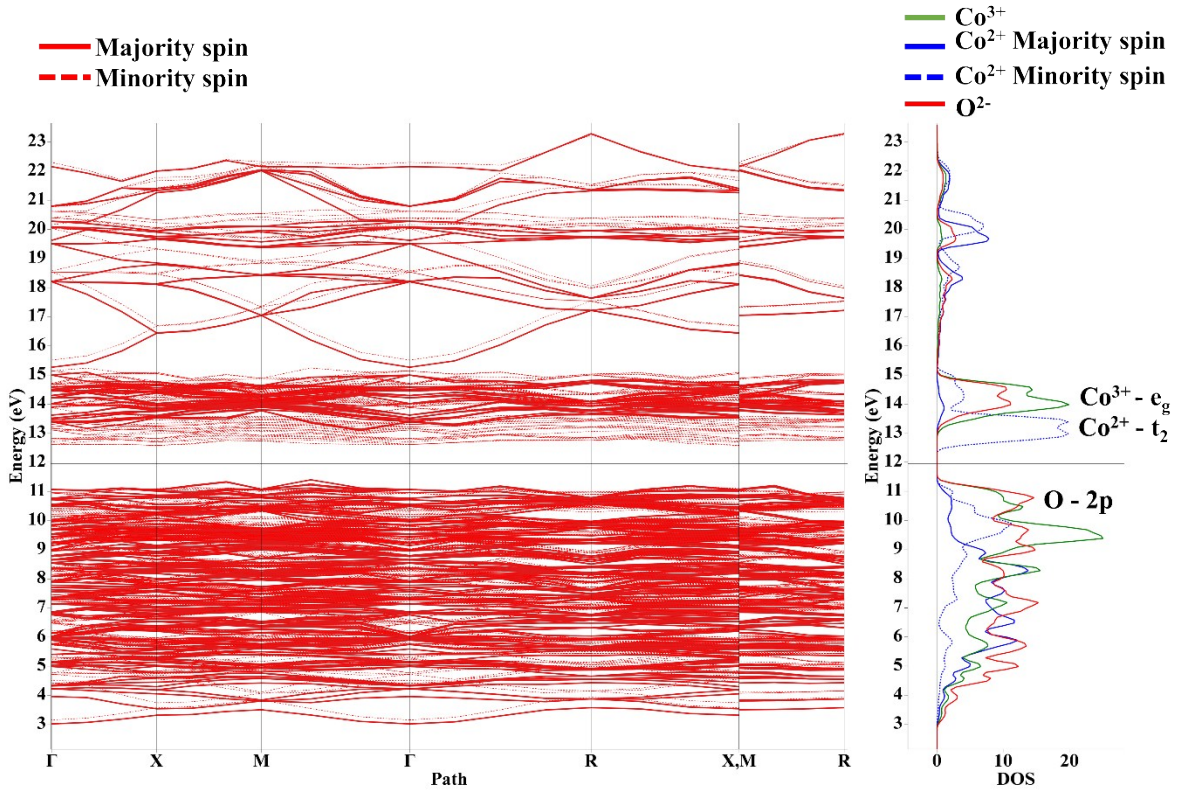

Figure S3. The PBE+U theoretical electronic band structure (a), and atomic projected density of states (DOS) (b) of the normal-spinel Co_3O_4.

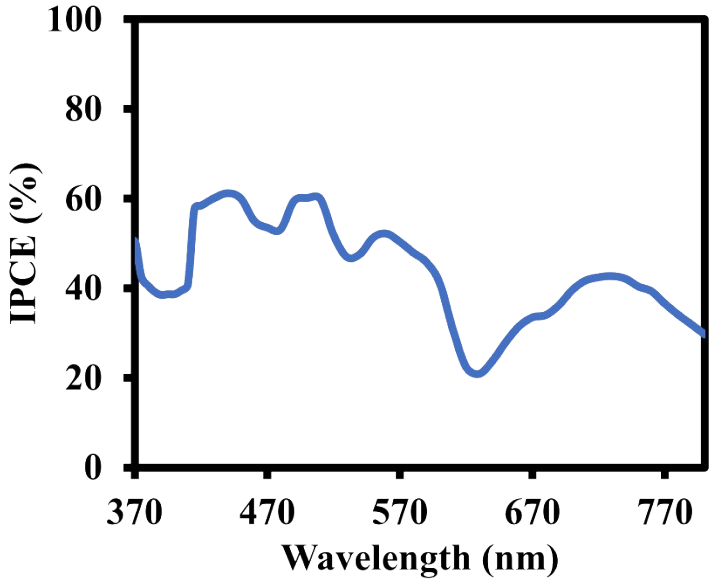

Figure S4. IPCE value of the Co_3O_4 photocathode for photoelectrochemical oxygen evolution reaction in 0.1M KOH.

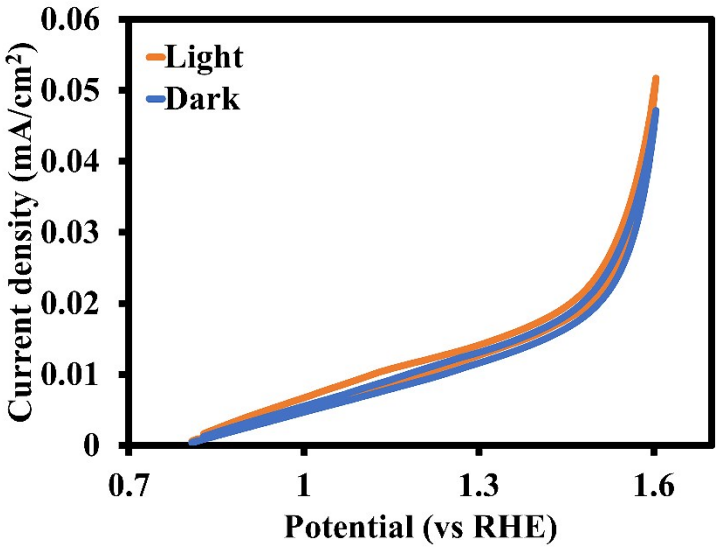

Figure S5. The CV curves of pure ITO under dark condition and light illumination.

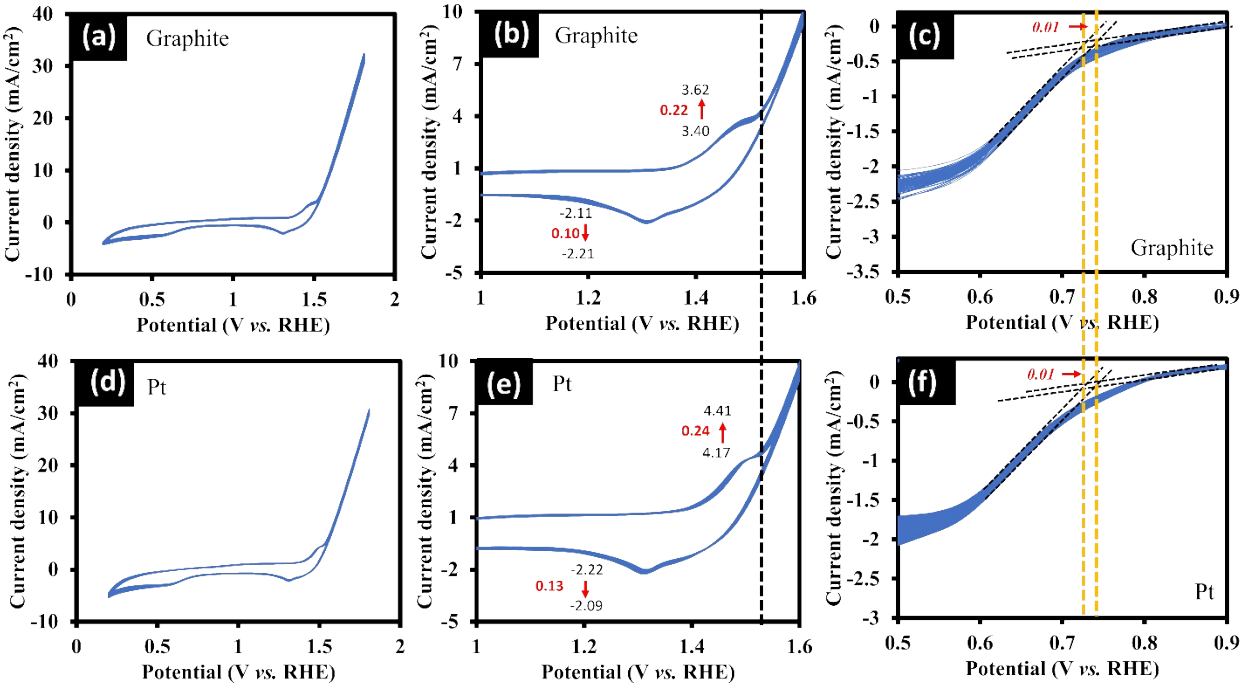

Figure S6. CVs (a, b, d, and e) and LSVs (c and f) of the Co_3O_4 catalyst coated on the glassy carbon electrode in 0.1 M KOH at a scan rate of 20 mV s^{-1} using graphite (a-c) and platinum (d-f) as the auxiliary electrodes.

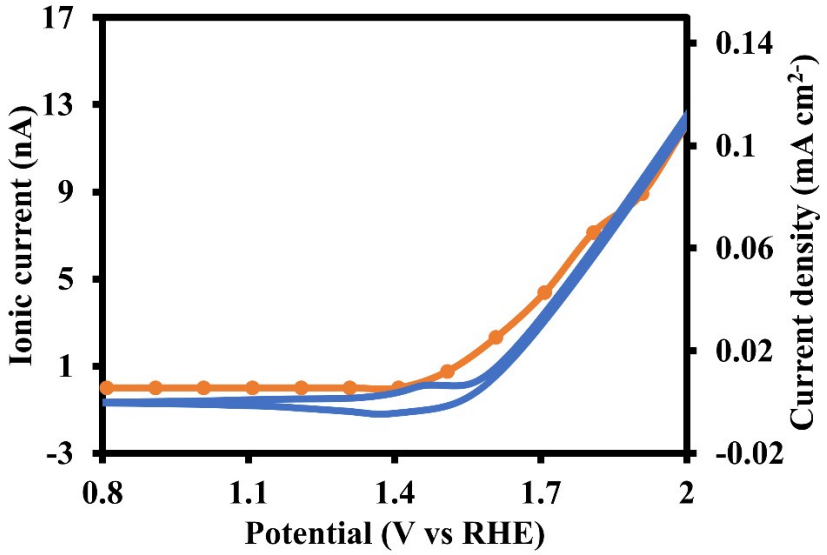

Figure S7. The ionic mass current of O_2 (m/z = 32) recorded during DEMS measurements of chronopotentiometry at 0.8-2.0 V (V *vs.* RHE).

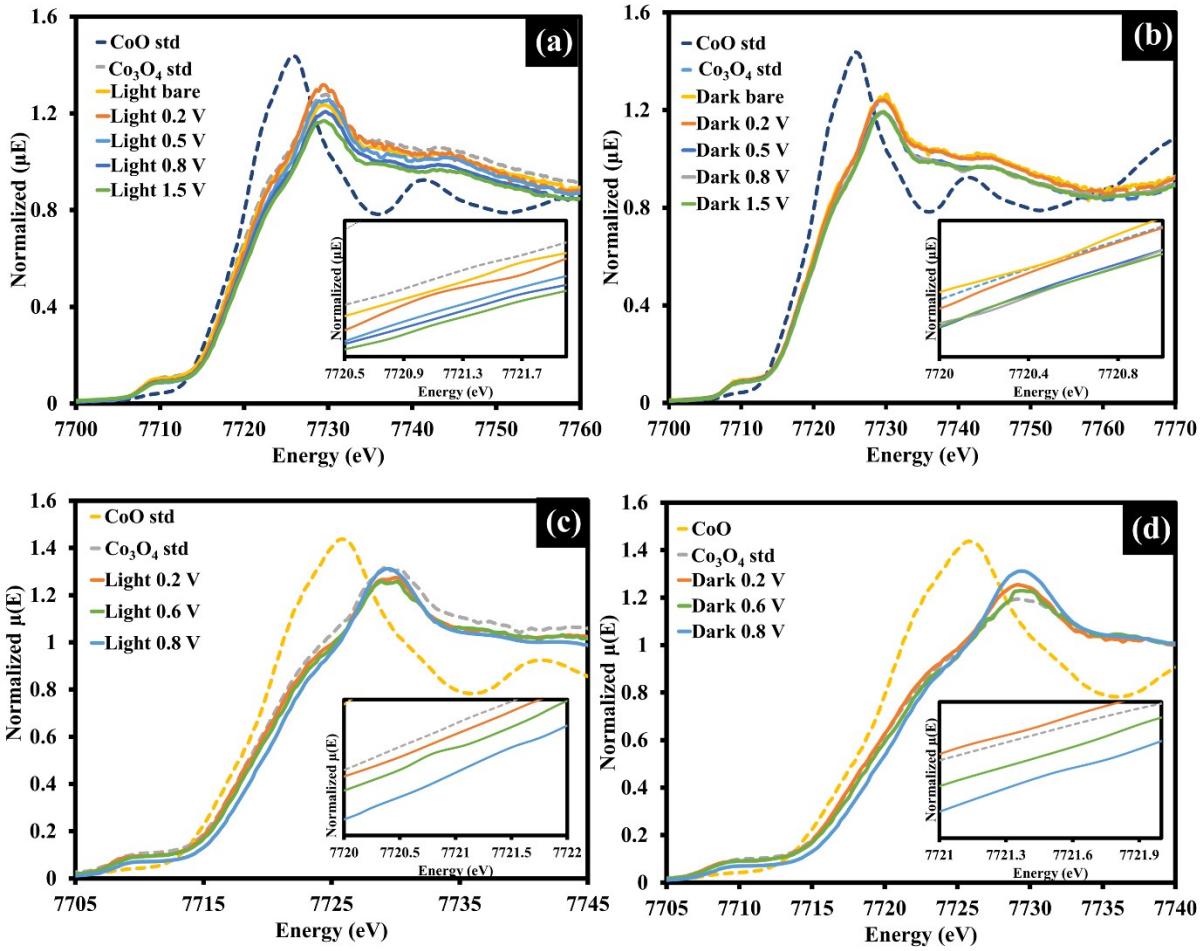

Figure S8. *Ex-situ* Co K-edge XANES spectra at different applied potentials of (a) OER process (1.2-2.5 V *vs*. RHE) under dark (b) OER process (1.2-2.5 V *vs*. RHE) under light (c) ORR process (0.8-0.2 V *vs*. RHE) under dark and (d) ORR process (0.8-0.2 V *vs*. RHE) under light

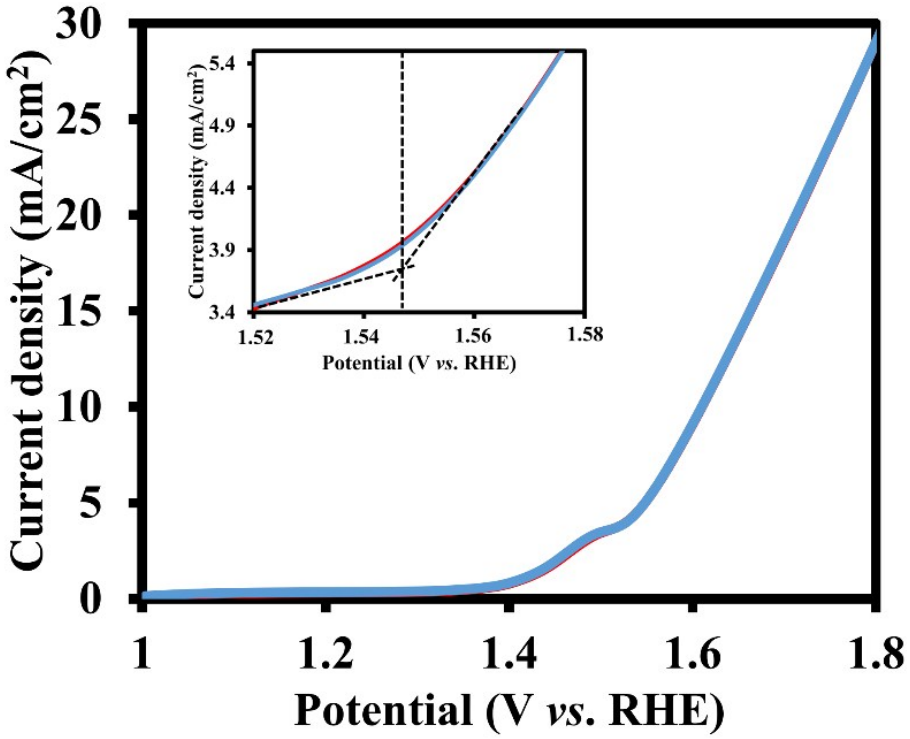

Figure S9. LSVs of the Co_3O_4 electrode in the basic solution (0.1 M KOH) at 20 mV s^{-1} under the temperatures of 26°C (blue) and 30°C (red).

As the solar light may heat up the electrolyte solution, the thermal effect on the electrochemical property of Co_3O_4 has been investigated. To clarify the thermal effect, we have set up an experiment to monitor the temperature change of the electrolyte solution under the light illumination using a solar simulator (Newport, Model 67005 sun simulator AM 1.5G/ 100 mW cm^{-2}) for 2 hours as compared to that under dark condition. Note, the distance between the light source and the electrochemical cell is 10 cm. The purge 99.99% oxygen gas was allowed to flow continuously through the cell as the real set up for ORR and zinc-air battery. The experiment has been video-recorded for 2 hours to see the temperature change. The result shows that the electrolyte solution temperature has increased from 26 $\pm$ 0.5 ˚C (under dark condition) to 30 $\pm$ 1.5 ˚C (under light illumination, AM 1.5G/ 100 mW cm^{-2}). The temperature change here is considered as a very small change (*ca*. 4 °C) as compared with other publications.[17, 18]

However, to further clarify the thermal effect of the increased temperature by *ca.* 4 ˚C on the electrochemical performance of Co_3O_4, the LSVs towards the OER of the Co_3O_4 electrode in the basic solution (0.1 M KOH) at 26 ˚C and 30 ˚C (**Figure** R2) were carried out. We have found that the LSVs at both systems (26 ˚C and 30 ˚C) are almost the same. Thus, we can neglect the thermal effect resulting from the light irradiation on our electrochemical performance in this work.

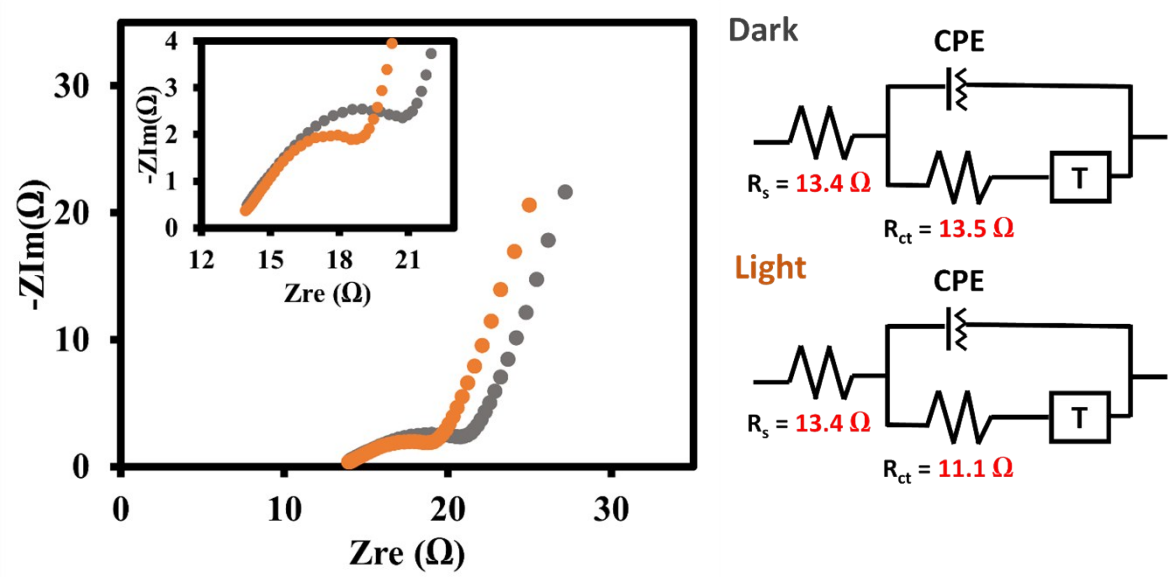

Figure S10. Nyquist plots and normal Randle's circuit of the Co_3O_4 electrode *vs.* RHE in 0.1 M KOH in the presence (orange) and absence (gray) of light illumination.

To investigate the charge transfer resistance (R_{ct}) of Co_3O_4 under light illumination and under dark condition. Electrochemical impedance spectroscopy (EIS) was used. The frequency is a range from 100 kHz to 0.01 Hz at the . The Nyquist plot (Figure S10) presents the relation of imaginary impedance (Z'') and the real impedance component (Z'). A semicircle region at higher frequency indicates an electron transfer limit process, and a linear part at lower frequency corresponds to a diffusion process. This process is fitted in an equivalent circuit of Randles circuit, $R_s(C(R_{ct}Z_T)$. Here, a resistance of solution (R_s) has a similar value in both the presence and absence of light illumination which is *ca.*13.4 Ω confirming that the heat effect can be ignored. The diameter of the semicircle region relates to the amount of charge transfer resistance (R_{ct}). The R_{ct} value is decreased by *ca*. 2.4 Ω after light irradiation. These results exhibit the higher of the electrons/charge transfer rate under the light illumination due to the higher active species namely electron hole, $Co_3O_4^*$.

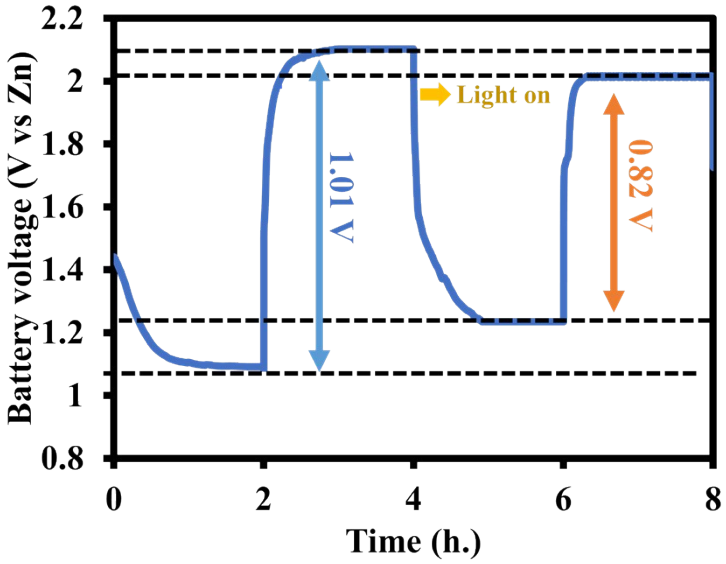

Figure S11. The long-term stability of Zn-air battery with a constant light on/off switch at 2 mA cm^{-2}

Figure S11 shows the long-term stability of the Zn-air battery using the Co_3O_4 cathode at a current rate of 2 mA cm^{-2}. The cell was set up as the same procedure as reported in the revised manuscript. When turning the light at the 2nd cycle, the charge/discharge potential gap reduces. The result is in good agreement with the report in the manuscript.

Table S1: The E_0 values and average oxidation numbers of Co_3O_4 during OER/ORR processes which is exposed to dark condition and light illumination.

	Samples	E_0	Average Oxidation numbers
Standard	CoO standard	7719.05	2.00+
	Co_3O_4 standard	7721.84	2.67+
OER process under dark	Co_3O_4 OCP	7721.19	2.60+
	Co_3O_4 1.2 V *vs* RHE	7721.89	2.80+
	Co_3O_4 1.5 V *vs* RHE	7723.46	3.24+
	Co_3O_4 1.8 V *vs* RHE	7724.14	3.43+
	Co_3O_4 2.5 V *vs* RHE	7724.24	3.45+
OER process under light	Co_3O_4 OCP	7721.68	2.80+
	Co_3O_4 1.2 V *vs* RHE	7722.88	3.07+
	Co_3O_4 1.5 V *vs* RHE	7725.33	3.76+

	Co_3O_4 1.8 V *vs* RHE	7726.19	4.00+
	Co_3O_4 2.5 V *vs* RHE	7726.19	4.05+
ORR process under dark	Co_3O_4 0.8 V *vs* RHE	7724.17	3.23+
	Co_3O_4 0.6 V *vs* RHE	7722.67	2.87+
	Co_3O_4 0.2 V *vs* RHE	7721.28	2.53+
ORR process under light	Co_3O_4 0.8 V *vs* RHE	7727.07	3.92+
	Co_3O_4 0.6 V *vs* RHE	7725.60	3.57+
	Co_3O_4 0.2 V *vs* RHE	7722.30	2.78+

Table S2: The OER and ORR catalytic activities of the Co-based materials of this work as compared with other publications

Materials	**Onset OER (V vs RHE)**	**Overpotential of OER to reach 10 mA cm^{2-} (mV)**	**OER corresponding Tafel values (mV dec^{1-})**	**Onset ORR (V vs RHE)**	**ORR corresponding Tafel values (mV dec^{1-})**	**Ref.**
Co_3O_4 nanoparticles (Light)	1.52	420	74.1	0.77	92.6	This work
Co_3O_4 nanoparticles (Dark)	1.58	600	109.3	0.72	102.2	This work
Co_3O_4 nanoparticles	1.75	620	73	0.40	77	REF[19]
Co_3O_4/ MnO_2	1.52	-	85.6	0.78	195	REF[20]
Cobalt Nanoparticles-embedded Carbon Nanotube/Porous	1.50	315	73.8	0.82	-	REF[21]

Carbon Hybrid Derived from MOF encapsulated Co_3O_4 (Co-CNT/PC)						
Co_3O_4/N-rmGO	1.50	310	67	0.88	42	REF[22]
Co_3O_4 nanofilm	1.61	461	96	0.64	78	REF[23]
Plasma-Engraved Co_3O_4 Nanosheets	1.45	300	68	-	-	REF[24]
Co@Co_3O_4/NC-1	1.58	410	91.1	0.82	86.2	REF[25]
RuO_2	1.50	309	52.5	-	-	REF[26]
Pt/C	7.908	-	-	0.808	-	REF[27]

Section 4: Calculations

4.1 Calculation of interlayer spacing or d-spacing

The interlayer spacing or d-spacing was calculated from the "Bragg's Law" equation;

$$n\lambda = 2d\sin\theta \quad \text{(S5)}$$

where n is a positive integer (n = 1 for our calculation), λ is the incident wavelength (for Cu Kα = 1.54056 Å), θ is the angle between the incident rays and the surface of the crystals (corresponding to 2θ from XRD pattern), and d is the lattice interplanar spacing of the crystal. The d-spacing of Co_3O_4 in this work was calculated from the dominant (311) plan of the spinel-type Co_3O_4 with $2\theta = 37.8358^o$

4.2 Calculation of band gap energy of Co_3O_4 from UV-Visible spectroscopy

The UV-Visible spectroscopy of Co_3O_4 was also being considered in this work to elucidate the band gap energy. The Co_3O_4 can absorb the light at the wavelength of *ca.* 755 and 440 nm in the visible light region. The Tauc plot relationship was plotted to determine the band gap energies of the Co_3O_4.

The optical band gap energy was determined by using Tauc relation;[28]

$$(\alpha h\nu)^n = k(h\nu - E_g) \quad \text{(S6)}$$

where α is the adsorption coefficient, $h\nu$ is the photon energy, k is a constant of material and E_g is the band gap energy. The n parameter can either be 1 or ½ for the direct or indirect band transition, respectively. The plot between $(\alpha h\nu)^n$ and $h\nu$ was used to determine the optical band gap of Co_3O_4 by using linear fitting to find the interception in x axis.

4.3 Calculation of average oxidation number from Ex-situ XAS

The average oxidation state of Co can be calculated using an empirical equation from the Co^{2+} (CoO standard) and $Co^{2.67+}$ (Co_3O_4 standard).

$$\text{Oxidation number} = 2.67\left(\frac{\Delta E\ of\ sample}{\Delta E\ of\ Co^{2.67+}\ and\ Co^{2+}}\right) + 2\left(1 - \frac{\Delta E\ of\ sample}{\Delta E\ of\ Co^{2.67+}\ and\ Co^{2+}}\right) \quad \text{(S7)}$$

4.4 Calculation of specific capacity

The specific capacity was calculated by following equation;[29]

$$\text{Specific capacity} = \frac{Ix\Delta t}{g_{zn}} \quad \text{(S8)}$$

where I is the applied current (mA), Δt is the discharging time (hour), and g_{zn} is the mass of consumed zinc.

REFERENCES

1. Lin, X.; Li, H.; Musharavati, F.; Zalnezhad, E.; Bae, S.; Cho, B.-Y.; Hui, O. K. S. *RSC Adv.* **2017,** 7, (74), 46925-46931.
2. Xu, R.; Zeng, H. C. *J. Phys. Chem. B.* **2003,** 107, (46), 12643-12649.
3. Li, B.; Xie, Y.; Wu, C.; Li, Z.; Zhang, J. *Mater. Chem. Phys.* **2006,** 99, (2), 479-486.
4. Li, J.; Li, X.; Luo, Y.; Cen, Q.; Ye, Q.; Xu, X.; Wang, F. *Int. J. Hydrog. Energy* **2018,** 43, (20), 9635-9643.
5. Wang, H.; Zhang, L.; Tan, X.; Holt, C. M. B.; Zahiri, B.; Olsen, B. C.; Mitlin, D. *J. Phys. Chem. C.* **2011,** 115, (35), 17599-17605.
6. Shao, Y.; Sun, J.; Gao, L. *J. Phys. Chem. C.* **2009,** 113, (16), 6566-6572.
7. Liu, X.; Yi, R.; Zhang, N.; Shi, R.; Li, X.; Qiu, G. *Chem. Asian J.* **2008,** 3, (4), 732-738.
8. Xie, H.; Tang, S.; Zhu, J.; Vongehr, S.; Meng, X. *J. Mater. Chem. A* **2015,** 3, (36), 18505-18513.
9. Tan, Y.; Gao, Q.; Li, Z.; Tian, W.; Qian, W.; Yang, C.; Zhang, H. *Sci Rep* **2016,** 6, 26460.
10. Paolo, G.; Stefano, B.; Nicola, B.; Matteo, C.; Roberto, C.; Carlo, C.; Davide, C.; Guido, L. C.; Matteo, C.; Ismaila, D.; Andrea Dal, C.; Stefano de, G.; Stefano, F.; Guido, F.; Ralph, G.; Uwe, G.; Christos, G.; Anton, K.; Michele, L.; Layla, M.-S.; Nicola, M.; Francesco, M.; Riccardo, M.; Stefano, P.; Alfredo, P.; Lorenzo, P.; Carlo, S.; Sandro, S.; Gabriele, S.; Ari, P. S.; Alexander, S.; Paolo, U.; Renata, M. W. *Journal of Physics: Condensed Matter* **2009,** 21, (39), 395502.

11. Kresse, G.; Joubert, D. *Physical Review B* **1999,** 59, (3), 1758-1775.
12. Perdew, J. P.; Burke, K.; Ernzerhof, M. *Physical Review Letters* **1996,** 77, (18), 3865-3868.
13. Perdew, J. P.; Ernzerhof, M.; Burke, K. *The Journal of Chemical Physics* **1996,** 105, (22), 9982-9985.
14. Anisimov, V. I.; Zaanen, J.; Andersen, O. K. *Physical Review B* **1991,** 44, (3), 943-954.
15. Chen, J.; Wu, X.; Selloni, A. *Physical Review B* **2011,** 83, (24), 245204.
16. Vaz, C. A. F.; Henrich, V. E.; Ahn, C. H.; Altman, E. I. *Journal of Crystal Growth* **2009,** 311, (9), 2648-2654.
17. Dias, P.; Lopes, T.; Andrade, L.; Mendes, A. *Journal of Power Sources* **2014,** 272, 567-580.
18. Lokhande, C. D.; Pawar, S. H. *Solar Energy Materials* **1982,** 7, (3), 313-318.
19. Monteverde Videla, A. H. A.; Stelmachowski, P.; Ercolino, G.; Specchia, S. J. J. o. A. E. *ChemSusChem* **2017,** 47, (3), 295-304.
20. Elumeeva, K.; Kazakova, M. A.; Morales, D. M.; Medina, D.; Selyutin, A.; Golubtsov, G.; Ivanov, Y.; Kuznetzov, V.; Chuvilin, A.; Antoni, H.; Muhler, M.; Schuhmann, W.; Masa, J. *Nanoscale* **2018,** 11, (7), 1204-1214.
21. Dou, S.; Li, X.; Tao, L.; Huo, J.; Wang, S. *Chemical Communications* **2016,** 52, (62), 9727-9730.
22. Liang, Y.; Li, Y.; Wang, H.; Zhou, J.; Wang, J.; Regier, T.; Dai, H. *Nature Materials* **2011,** 10, 780.
23. He, Y.; Zhang, J.; He, G.; Han, X.; Zheng, X.; Zhong, C.; Hu, W.; Deng, Y. *Nanoscale* **2017,** 9, (25), 8623-8630.
24. Xu, L.; Jiang, Q.; Xiao, Z.; Li, X.; Huo, J.; Wang, S.; Dai, L. **2016,** 55, (17), 5277-5281.
25. Aijaz, A.; Masa, J.; Rösler, C.; Xia, W.; Weide, P.; Botz, A. J. R.; Fischer, R. A.; Schuhmann, W.; Muhler, M. **2016,** 55, (12), 4087-4091.
26. Du, G.; Liu, X.; Zong, Y.; Hor, T. S. A.; Yu, A.; Liu, Z. *Nanoscale* **2013,** 5, (11), 4657-4661.
27. Xu, N.; Liu, Y.; Zhang, X.; Li, X.; Li, A.; Qiao, J.; Zhang, J. *Sci Rep* **2016,** 6, 33590.
28. Pinaud, B. A.; Chen, Z.; Abram, D. N.; Jaramillo, T. F. *J. Phys. Chem. C.* **2011,** 115, (23), 11830-11838.
29. Pandit, B.; Dubal, D. P.; Gómez-Romero, P.; Kale, B. B.; Sankapal, B. R. *Sci Rep* **2017,** 7, 43430.